Electrochemical Deposition of Copper on Epitaxial Graphene

Ivan Shtepliuk [1,2,*], **Mikhail Vagin [1,3]** and **Rositsa Yakimova [1]**

[1]   Semiconductor Materials, Department of Physics, Chemistry and Biology-IFM, Linköping University,
     SE-58183 Linköping, Sweden; mikhail.vagin@liu.se (M.V.); rositsa.yakimova@liu.se (R.Y.)
[2]   Frantsevich Institute for Problems of Materials Science, NASU—National Academy of Sciences of Ukraine,
     142 Kyiv, Ukraine
[3]   Laboratory of Organic Electronics, Department of Science and Technology, Linköping University,
     SE-60174 Norrköping, Sweden
[*]   Correspondence: ivan.shtepliuk@liu.se; Tel.: +46-13282528

Abstract: Understanding the mechanism of metal electrodeposition on graphene as the simplest building block of all graphitic materials is important for electrocatalysis and the creation of metal contacts in electronics. The present work investigates copper electrodeposition onto epitaxial graphene on 4H-SiC by experimental and computational techniques. The two subsequent single-electron transfer steps were coherently quantified by electrochemistry and density functional theory (DFT). The kinetic measurements revealed the instantaneous nucleation mechanism of copper (Cu) electrodeposition, controlled by the convergent diffusion of reactant to the limited number of nucleation sites. Cu can freely migrate across the electrode surface. These findings provide fundamental insights into the nature of copper reduction and nucleation mechanisms and can be used as a starting point for performing more sophisticated investigations and developing real applications.

Keywords: epitaxial graphene; copper; redox reaction; electrodeposition; voltammetry; chronoamperometry; DFT

1. Introduction

Copper (Cu) deposition is one of the key processes in the electronic industry for circuit interconnections, increasingly replacing aluminum [1]. The electrodeposition of copper has the advantages over physical and chemical vapor deposition methods since it seems to be cheapest and best method to fill vias and trenches. Moreover, copper is one of the most-investigated metal catalysts, stipulating studies of electrodeposition on a variety of carbon materials, especially graphite [2–4].

The electronic conductivity of graphite is established due to the planar conjugation of the sp^2 bonds in a single graphene sheet as a primary building block of all graphitic materials. This defines a significant anisotropy of the density of states (DOS) for in-plane and out-of-plane (edge and basal planes, correspondingly) electronic conduction, which is the origin of the duality in the general properties of all graphitic materials [5,6]. The use of macroscale defect-free graphene sheets [7] allows for the avoidance of contributions from the reactive edge plane of high DOS. In the past decade, huge efforts have been made to conceptualize graphene–copper material hybridization for practical applications [8–13]. Particularly, it was discovered that the addition of graphene to the copper matrix can improve the mechanical and electrical properties of Cu, causing a significant increase in the electrical conductivity, Young's modulus, shear modulus, and Vickers hardness as well as a reduction in the thermal expansion coefficient [8–11]. The aforementioned advantages create excellent prerequisites for copper–graphene (Cu–Gr) composites to be used as reliable interconnection materials, electrical contact materials for

ultrahigh-voltage circuit breakers and printed electronics. The enhanced conductivity of the Cu–Gr composite also determines its exploitation as a high-performance counter electrode in solar cells [12,13]. Furthermore, due to the larger heat transfer coefficient and higher corrosion resistance of Cu–Gr hybrids in 3.5% NaCl medium when compared to pure copper [14–18], these materials are very promising for engineering applications (for instance, anti-corrosion coatings) in sea water and for heat transfer applications, respectively. Copper–graphene nanohybrids were, however, recognized and appreciated mainly for their role in the development of efficient catalytic and ultrasensitive detection technologies. The benefits gained from the interaction between graphene-based materials and copper have been used for reduction of 4-nitrophenol (4-NP) to 4-aminophenol [19,20], oxidation of hydrazine [21,22], electro-oxidation of methanol [23], hydrogen evolution reaction (HER) [24,25], the electrochemical reduction of CO_2 to ethanol [26], oxidative carbonylation of methanol [27], CO_2 cycloaddition to propylene oxide (PO) [28], formic acid synthesis by CO_2 hydrogenation [29] and CO_2 electroreduction for methane and methanol production [30]. Beyond the issue of high-performance catalysts, it is worth mentioning that Cu–Gr composites have also been applied to the electrochemical detection of ascorbic acid and dopamine [31], organophosphorus pesticide [32], heavy metals [33,34], glucose [35–39], chlorophenol pollutants in wastewater [40], hydroquinone and catechol [41], nitrite [42,43], nitrogen dioxide (NO_2) [44] and hydrogen peroxide (H_2O_2) [45]. Numerous density functional theory (DFT) calculations shed light on the adsorption of different gases (H_2S [46,47], CO [48], CO_2 [49], N_2O [50], H_2 [51–53]) and organic molecules [54–56] onto Cu-decorated/doped/anchored graphene, thereby providing the solid theoretical background that is required to design efficient sensing devices.

Until now we have been giving an overview of most relevant applications of copper–graphene composite materials. However, there is another aspect of mutual interplay between graphene and copper that needs to be addressed: the detection and removal of Cu^{2+} ions in/from potable water. Even though Cu is the third most abundant transition metal in the human body and it is vitally important for human health, an excess of copper ions can cause cirrhosis of the liver in children, Wilson's disease, Alzheimer's disease, etc. [57,58]. For this reason, the development of ultra-sensitive and selective methods for the monitoring and determination of trace Cu^{2+} ions in water is highly demanded. Since graphene enables the detection of single molecules accommodated on its surface [59], it attracts a lot of attention as a highly sensitive and biofriendly material for environmental sensorics [60], including the fast and real-time detection of Copper ions [61]. Two strategies in such a direction have been implemented so far: (i) electrochemical sensing by electrodes covered with functionalized graphene-based materials (reduced graphene oxide, graphene oxide, graphene quantum dots) [62–65] and (ii) optical sensing using colorimetric and fluorescent probes based on graphene derivatives [66–74]. Both approaches present some limitations, mainly linked to the instability and complicated preparation procedure of the working electrode or fluorescence probe, which typically involves surface functionalization and multistage chemical reactions. In most cases, such a functionalization can increase the toxicity of a sensitive component and is, therefore, less desired.

Exploiting epitaxial graphene grown on SiC (epitaxial graphene (EG)/SiC) using the high-temperature sublimation technique is regarded as an alternative strategy for sensing platform development. Due to evident advantages over other graphene family materials (namely, its large surface area free of functional groups, high quality of monolayer graphene, thickness uniformity, wide potential window, high signal-to-noise ratio, transfer-free technology, and direct sublimation growth without precursors [75–77]), epitaxial graphene has been tested with promising results for the real-time detection of Pb^{2+} ions in aqueous solutions (with a detection limit far below the WHO's permissible level for lead in drinking water) through performing square-wave anodic stripping voltammetry and response–recovery measurements [78,79]. Inspired by this, we have recently extended our activities beyond lead detection to include the investigation of the electrochemical behavior of the Hg^{2+}/Hg^0 redox couple at the epitaxial graphene working electrode [80]; now, we are aiming to elucidate the nature of the copper electroreduction at the epitaxial graphene surface. Since this issue is very poorly investigated in the literature, in-depth investigations at an atomistic level are still needed to deal with

the problem. In this regard, complementary electrochemical and theoretical studies of the graphene–Cu system presented here may provide critical information on the Cu kinetics, diffusion, adsorption and sensing mechanisms, thereby facilitating the development of a real-time detection platform. Leaving aside the Cu^{2+} detection by using graphene, it should be recalled that a holistic understanding of the interplay between epitaxial graphene and copper is essential not only for sensing applications, but also for catalytic and electrical applications, due to the mutually reinforcing character of the graphene–Cu pair.

In this report, the electrodeposition of copper on epitaxial graphene has been investigated in acidic environment. The electrodeposition of copper occurs by instantaneous nucleation at a limited number of sites, via a bi-electronic reduction bypassing of Cu^{1+} intermediates at a significant overpotential with respect to the process in graphitic materials. The computational methods showed coherence with the experimental observations.

2. Materials and Methods

2.1. Reagents

Copper (II) sulfate and perchloric acid were purchased from Sigma (Stockholm, Sweden) and used as received. Experiments were carried out with Milli-Q water from a Millipore Milli-Q system.

2.2. Samples and Processes

An Autolab type III potentiostat (Autolab, EcoChemie, Utrecht, Netherlands) was used for the electrochemical measurements. An Ag/AgCl electrode in 3 M KCl and a platinum wire were employed as reference and counter electrodes, respectively, for all measurements.

The samples of nominally monolayer epitaxial graphene (EG) on SiC (substrate area 7×7 mm^2 and thickness 0.4 mm) were obtained from Graphensic AB and produced by the high temperature thermal decomposition of the Si-face (0001) 4H-SiC substrate (7×7 mm^2) in an argon atmosphere using an inductively heated graphite container with a well-controlled temperature profile [81]. Most of the substrate surface is coated with monolayer graphene after graphenization, while the fraction of bilayer graphene islands is negligibly small, which is evidenced by optical reflectance mapping [82]. The samples of epitaxial graphene were used as a working electrode in the open electrochemical cell obtained from Redoxme AB [83]. The cell consisted of a cup of 300 μL with a 2 mm diameter hole and a Vitron o-ring on the bottom. The EG sample was fixed under the hole with the o-ring using screws on the lid. A dry contact for the EG was formed by an aluminum adhesive. The mounted EG sample was kept inside the cell during all wet measurements and procedures in order to avoid sample drift.

The electrolyte solution was prepared from ultrapure 0.1 mol·L^{-1} HClO$_4$, 0.1 mM Cu^{2+} (the purity of copper sulfate, CuSO$_4$, was higher than 99%), and Milli-Q water. The non-complexing character of the perchlorate ions (ClO^{4-}), with respect to metal cations in aqueous solutions [84–86], suggests that the cyclic voltammetry (CV) measurements will enable us to gain insights into Cu-involved oxidation–reduction reactions, rather than reactions involving more complicated chemical complexes. To explore the Cu redox behavior and kinetics at the working electrode, we exploited the quite concentrated aqueous solution of Cu salt to ensure an intense electrochemical signal. The scan rate was 20 mV/s. The electrochemical reactions are expected to occur at the nominal electrode area of 3.1 mm^2. To elucidate the nature of the Cu kinetics, current–time transients were recorded during the early stages of Cu electrodeposition on Gr/SiC.

2.3. Computational Methods

The Scharifker–Hills approach [87] has been applied to shed light on the nucleation mechanism. The electrochemistry of Cu at the graphene surface was also investigated through in-depth functional theory (DFT) calculations performed by using the Gaussian 16 Rev. B.01 package [88]. The C$_{150}$H$_{30}$ structure was chosen as a model of graphene. Since, in aqueous solution, the water molecules

demonstrate a strong tendency to attach to the metal cation and to form the first coordination sphere (primary solvation shell), in the present paper, we consider the interaction of the $[Cu(H_2O)_6]^{2+}$ complexes with graphene, and their reduction to $[Cu(H_2O)_6]^0$ species. All calculations were carried out using the PBE1PBE level of theory, with empirical dispersion corrections [89,90]. The 6–31G(d,p) basis set was used for carbon, oxygen, and hydrogen atoms, while the basis set developed by the Stuttgart–Dresden–Bonn group (SDD) was utilized for the Cu [91]. Noncovalent interaction (NCI) analysis was performed using the Multiwfn program to better understand the Cu–carbon bonding characteristics [92].

3. Results and Discussion

The voltammetry of epitaxial graphene (Figure 1) in the pure supporting electrolyte does not show any faradaic current in the double layer region of potentials (between +0.5 and −0.4 V). The larger negative potentials (below −0.6 V) applied on epitaxial graphene in pure acidic electrolytes were characterized by the appearance of faradaic currents due to the appearance of a hydrogen evolution reaction. The addition of copper ions to the thousand-times excess of background electrolytes led to the increase in capacitive currents (ca. 2.5 times at 0.5 V). This manifests the strong adsorption of di-cations on epitaxial graphene [77,78,93]. In parallel, the redox phenomena associated with the electrodeposition and dissolution of the metal species became explicit. The voltammetry scan in the negative direction shows the appearance of an intensive cathodic process at potentials below −0.2 V. Being a poor complexing ion, perchlorate disables the stabilization and appearance of Cu^{1+}-based intermediates, which is illustrated by the absence of any redox processes at the higher potentials [94,95]. This implies that the copper electrodeposition on epitaxial graphene proceeds via single, irreversible bi-electronic reduction. The nucleation loop observed for the cathodic process is assigned to the new phase formation [96]. Taking into account the differences in the concentration of copper ions as well as the irreversible (non-Nernstian) character of the deposition process [3], the current density of the nucleation loop reaches values comparable with copper electrodeposition on glassy carbon [3] and pyrolytic graphite [4] at the potentials shifted on ca. 400 mV in a negative direction. This overpotential illustrates the typically slower kinetics of the generalized faradaic process on an epitaxial graphene monolayer in comparison with the common bulk graphitic interfaces [97] contributed by reactive graphene edges.
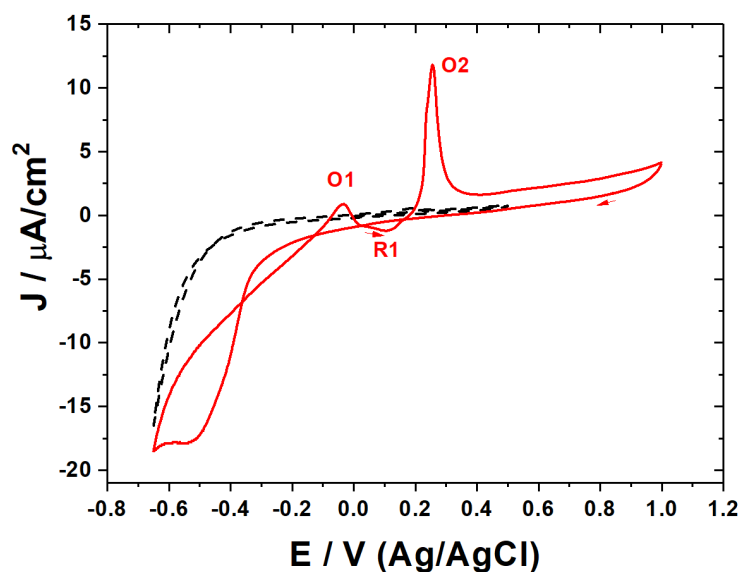
Figure 1. Cyclic voltammograms related to the electrodeposition and stripping of copper on the epitaxial graphene (in absence and in presence 0.1 mM Cu^{2+}, as dashed black and solid red curves, respectively; 0.1 M $HClO_4$, scan rate 20 mV·s^{-1}).

The voltammetry scan in the positive direction showed the appearance of discrete steps of dissolution (stripping) of the copper deposits. The direction-dependent voltammetry response illustrates the difference between the pristine and copper-modified epitaxial graphene monolayer presented at potentials higher than 0.5 and lower than −0.5 V, respectively. The oxidation peak current (O1), located at −0.03 V. corresponds to the single-electron oxidation of metallic copper to Cu^{1+}. Further increases in the applied potential in a positive direction led to the unusual appearance of the negative current (R1) at 0.1 V. In contrast to the kinetically slow electrochemical deposition of copper on the epitaxial graphene monolayer, the aforementioned instability of Cu^{1+} might enable an exergonic (non-faradaic) route towards the metallic copper at the surface via fast disproportionation. Here, the state of the surface is not pristine yet. As soon as the copper ions undergo the faster reduction in metallic copper in comparison with bare carbon [96], the metallic copper might act as an electrocatalyst for the reduction, in comparison with epitaxial graphene originating the appearance of the negative currents. Further increases in potential in a positive direction showed the appearance of the sharp peak current typical in complete oxidation to Cu^{2+} ions. The scenario of the electrode processes was repeated with continuous voltammetry cycling.

We performed DFT calculations in order to assay the reduction thermodynamics. The Cu^{2+} ion was considered, when coordinated with six water molecules [98], energetically, the most favorable complex (Figure 2a). All calculations were performed using the aquo complexes of copper species, because the intrinsic or extrinsic solvent models did not give satisfactory results.
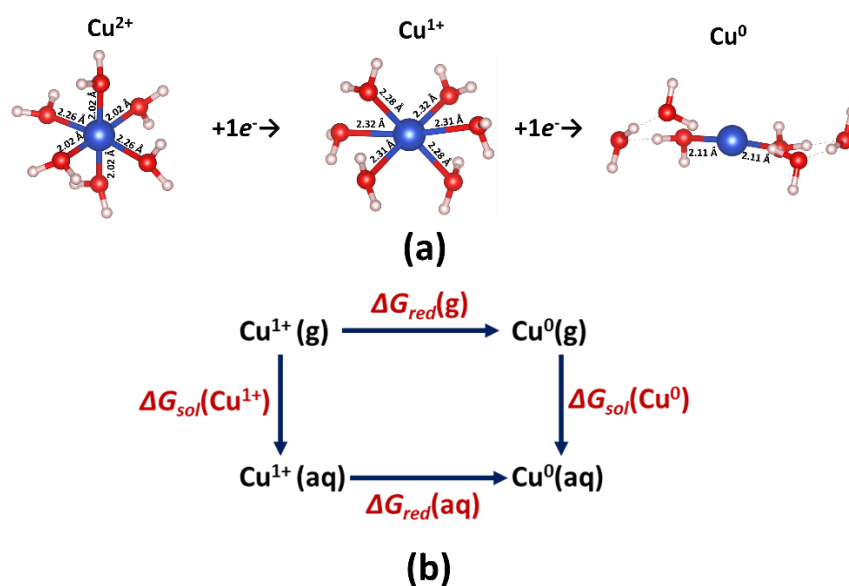
Figure 2. (**a**) Structures of the copper (Cu) complexes: $[Cu(H_2O)_6]^{2+}$, $[Cu(H_2O)_6]^{1+}$, $[Cu(H_2O)_6]^{0}$. The numbers are bond lengths in Å. Light pink, blue and red spheres represent H, Cu and O atoms, respectively. (**b**) The Born–Haber cycle for the calculation of the potential reductions in $[Cu(H_2O)_6]^{1+}$ to $[Cu(H_2O)_6]^{0}$.

The sequential additions of water molecules yielded the stabilization of all considered particles, computed as a decrease in the electron acceptor reactivity (Figure S1, Supporting Information) and the Hirshfeld charge on the Cu species (Figure S2, Supporting Information). The aquo complex has disordered octahedral geometry (Jahn–Teller distortion) with four short (2.02 Å) and two elongated Cu–O bonds (2.26 Å). According to the Hirshfeld charge population analysis, the charge located on the copper atom is equal to $+0.601e^-$. The addition of a first electron yielded the aquo Cu^+ complex with a smaller Hirshfeld charge on the copper atom (+0.216) and all elongated Cu–O bonds. The addition of the second electron led to the formation of metallic copper, confirmed by the negligibly small Hirshfeld charge on the copper atom ($+0.005e^-$) and the destruction of the octahedral geometry.

The equilibrium potential of the mono-electronic redox couple $[Cu(H_2O)_6]^{1+}/[Cu(H_2O)_6]^0$, estimated by applying the Born–Haber methodology (Figure 2b) [99], was −0.59 V, which agrees well with the experimental position of the metallic copper deposition. On the contrary, the computed value of the equilibrium potential of the bi-electronic redox couple $[Cu(H_2O)_6]^{2+}/[Cu(H_2O)_6]^0$ was −0.93 V, which is too low in comparison with the observed potential. This might imply that the copper deposition proceeds via mono-electronic reduction, followed by the fast exergonic disproportionation of unstable Cu^{1+} intermediates.

The irreversible process of copper deposition was quantified by the dynamic electrochemical measurements employing Scharifker–Hills formalism [87]. Current transients recorded at different deposition potentials (Figure 3a) are contingent on the applied potential pulse. The short-elapsed times (ca. 0.2 s) are characterized with the equilibration of the electrical double layer at the epitaxial graphene–electrolyte interface. The longer times are characterized with a faradaic process of copper electrodeposition (Inset in Figure 3a). Specifically, the potential pulses of −0.39 and −0.4 V are featured with non-monotonous current transients indicative of the three-dimensional (3D) nucleation process with diffusion-controlled growth [100] which enable analysis of the nucleation mechanism at the early stages of the electrodeposition [87]. The behavior of the active sites available for the formation and growth of the metal nuclei differentiates the two distinctive cases of the nucleation process. Accordingly, the instantaneous nucleation implies the maintenance of the convergent diffusion of the reactant on the limited number of nuclei. On the contrary, progressive nucleation relies on the increase in the number of nuclei yielding the quick establishment of overlapped planar reactant diffusion. The theoretical current transients obey the following equations:

$$\begin{cases} \left(\frac{j_{inst}}{j_{max}}\right)^2 = 1.9542\left(\frac{t}{t_{max}}\right)^{-1}\left\{1 - \exp\left[-1.2564\left(\frac{t}{t_{max}}\right)\right]\right\}^2 \\ \left(\frac{j_{prog}}{j_{max}}\right)^2 = 1.2254\left(\frac{t}{t_{max}}\right)^{-1}\left\{1 - \exp\left[-2.3367\left(\frac{t}{t_{max}}\right)^2\right]\right\}^2 \end{cases} \quad (1)$$

where t and t_{max} are the elapsed and maximum times, respectively; j_{inst}, j_{prog} and j_{max} are the current densities for instantaneous and progressive nucleation, and maximum current density, respectively. The initial kinetics of the copper electrodeposition obeys the three-dimensional instantaneous nucleation model (Figure 3b), which is likely the general mechanism for the metal's electrodeposition on epitaxial graphene monolayer, since the same growth kinetics was observed during electrodeposition of lead [101] and mercury [80]. This implies that metal electrodeposition on epitaxial graphene happens on a limited number of active sites.

The diffusion coefficient of copper ions as a reactant can be estimated from the current transients using the following relationship [102]:

$$D = \frac{j_{max}^2 \, t_{max}}{0.1629 \cdot (z \cdot F \cdot C)^2} \quad (2)$$

where the t_{max} is maximum time, corresponding to the maximum current j_{max}, z is the valency of the metal ion (+2 in the case of divalent species), F is the Faraday constant (96 485 C/mol), C is the reactant concentration (10^{-7} mol/cm^3). The values of the diffusion coefficient were 4.97×10^{-5} cm^2/s and 5.32×10^{-5} cm^2/s (at −0.39 and −0.40 V, respectively), which is higher than reported for glassy carbon (~0.4–0.8 × 10^{-5} cm^2/s) [3]. The nuclei population density on epitaxial graphene monolayer was determined by using the following formula:

$$N_0 = 0.065\left(\frac{1}{8\pi CV_m}\right)^{1/2}\left(\frac{nFC}{I_{max}t_{max}}\right)^2 \quad (3)$$

where n is the number of electrons involved, V_m is the molar volume. N_0 was estimated to be as high as a 1.55×10^6 cm^{-2} and 1.38×10^6 cm^{-2} (at −0.39 and −0.40 V, respectively), which is comparable with data from the literature [3].
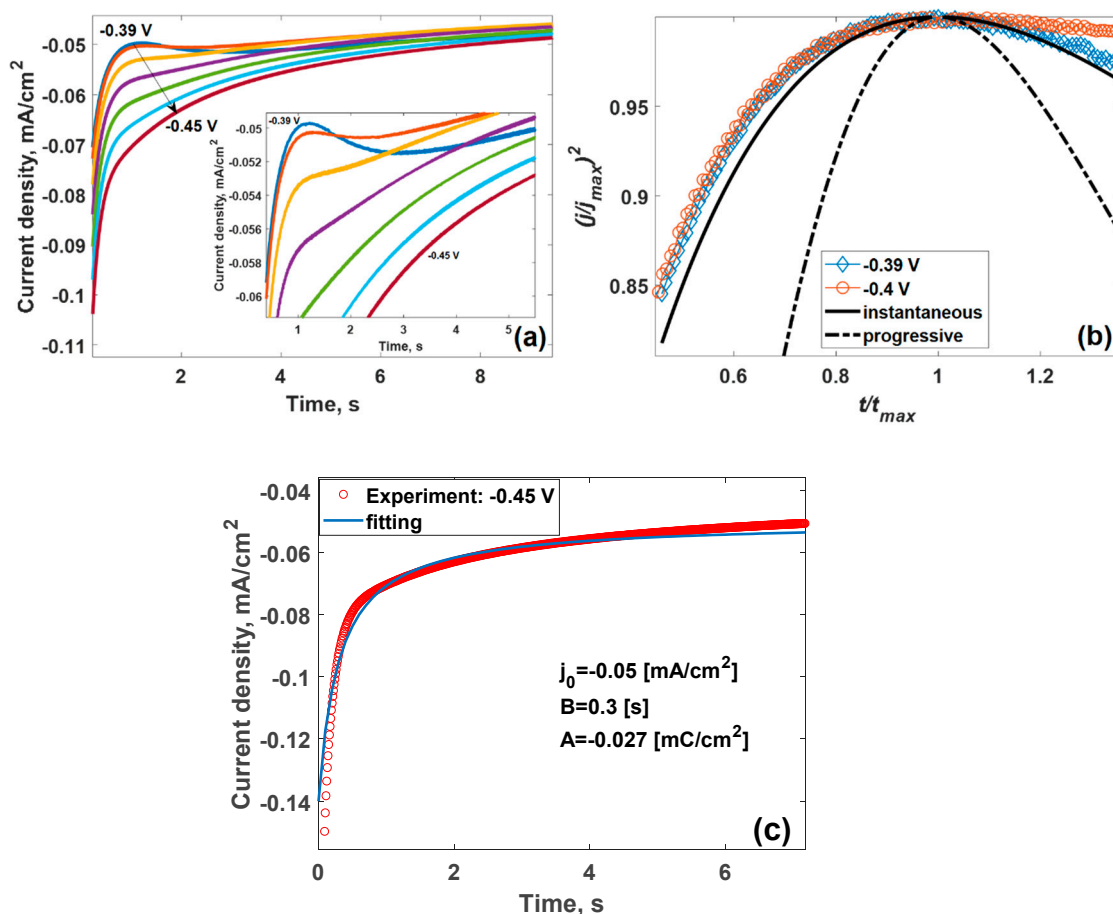
Figure 3. (**a**) Potentiostatic current transients recorded on epitaxial graphene recorded at the cathodic potential pulses of different amplitudes (resting potential 0.5 V; 0.1 M $HClO_4$, 0.1 mM Cu^{2+}). Insert: zoomed current transients; (**b**) comparison of the dimensionless experimental (open symbols) and theoretical transients for instantaneous (bold solid black curve) and progressive (bold dashed–dotted curve black curve) nucleation; (**c**) experimental current transient recorded at −0.45 V (red circles) and Elovich fitting curve (blue solid curve), respectively.

The change of the deposition potential towards more negative values led to the appearance of monotonous current transients (Figure 3a) assigned to the loss of the diffusion control and the appearance of chemisorption phenomena due to the double-layer effect at the electrode surface [103], which can be well described by the modified Elovich equation [103]:

$$J = \frac{A}{B + t} + j_L \qquad (4)$$

where A, B and j_L are fitting parameters. It was revealed that that the best fit can be achieved by using the following parameters as follows: $A = −0.027$ mC/cm^2, $B = 0.3$ s and $j_L = −0.05$ mA/cm^2 (Figure 3c).

To better understand the nature of the interaction between electro-reduced species with graphene under realistic conditions, we then simulated the two-stage reduction process by (i) adding one electron directly to the Cu^{2+} ion in the $[Cu(H_2O)_6]^{2+}$ complex adsorbed on graphene to form $[Cu(H_2O)_6]^{1+}$ and (ii) adding one more electron to the resulting $[Cu(H_2O)_6]^{1+}$ complex in order to form the neutral complex $[Cu(H_2O)_6]^0$. The result of the structural optimization is shown in Figure 4a. As a direct consequence of the reduction process, the six-coordinated water complex is broken, and all complex's components become weakly bonded to each other. Having a positive charge (according to Hirshfeld population analysis) of $+0.29e^-$, the Cu atom tends to occupy the top site (directly above the C atom) of the graphene, with an adsorption height of 2.7 Å. The results of the energy decomposition analysis,

based on forcefield (EDA-FF), presented in Table 1 showed that the interaction between copper and graphene was very weak and was dominated by dispersion forces, while a strong repulsion is expected between the water molecules and the Cu atom because these two fragments both have a positive charge.
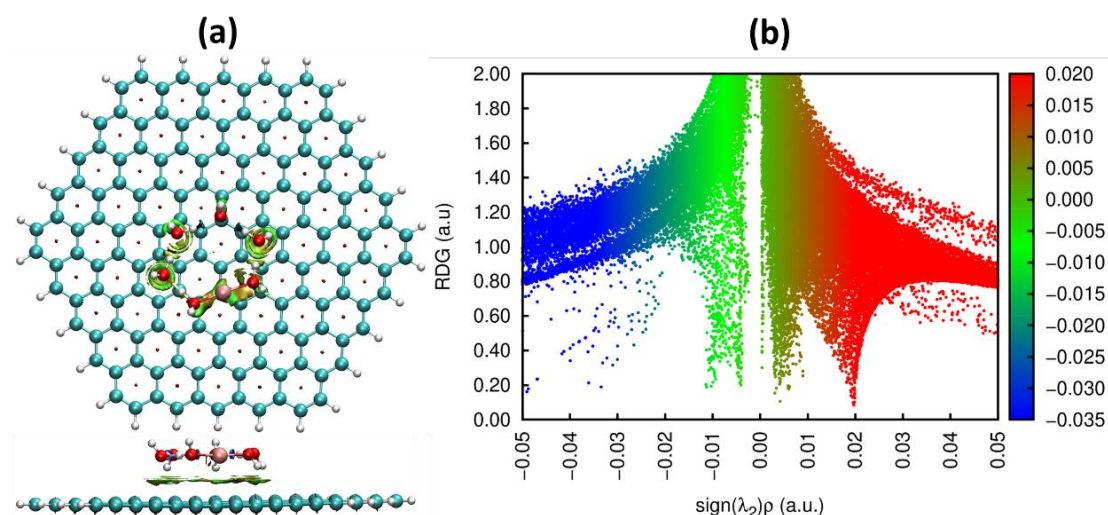
Figure 4. (**a**) Top and side view plots of the noncovalent interaction (NCI) iso-surface (reduced density gradient, RDG = 0.5) for reduced $[Cu(H_2O)_6]^0$ complex on graphene and (**b**) corresponding NCI diagram (RDG vs. $sign(\lambda_2)\rho$). The iso-surfaces are colored according to $sign(\lambda_2)\rho$ in the range −0.035–0.02 a.u. Red indicates the steric repulsion region; green (light brown) indicates the van der Waals interaction region, and blue implies the strong attractive interaction. Note: the optimization of the $[Cu(H_2O)_6]^0$ complex on graphene has been performed with consideration of solvent effect (water in our case) by using polarizable continuum model.

Table 1. Results of energy decomposition analysis.

Interaction between Fragments	Electrostatic, kJ/mol	Repulsion, kJ/mol	Dispersion, kJ/mol	Total Energy, kJ/mol
Graphene–Cu	0.00	1.33	−2.59	−1.26
Graphene–water	−3.58	42.38	−86.01	−47.21
Cu–water	0.00	420.21	−20.10	400.11

Noncovalent interaction (NCI) analysis enabled us to visualize the weak interaction between $[Cu(H_2O)_6]^0$ and graphene, which manifests itself as the green and light brown-colored nonbonding interaction areas located between copper and graphene in the vicinity of the top site (Figure 4a) and in the presence of two spikes within the $sign(\lambda_2)\rho$ region ranging from −0.01 to 0.01 a.u. (Figure 4b).

As was estimated by our DFT calculations, whenever the electro-reduced Cu species reach the graphene surface, they can freely diffuse along both considered diffusion paths with a small energy barrier of 35 meV (Figure 5a,b). Copper atoms tend to avoid occupation of the unfavorable hollow sites. It is interesting to note that the presence of the second copper atom (the already reduced and adsorbed Cu species) at the graphene surface significantly modifies the diffusion path due to the attractive interatomic interaction between neutral Cu species, making the Cu migration energetically favorable and promoting Cu clusterization. From a practical point of view, this means that, due to the favorable mass transfer and nucleation rate, the discrete diffusion zones of individual Cu nuclei will overlap very fast with time. For this reason, the cathodic current reaches a peak current maximum during the first two seconds and then decays slowly (as was demonstrated in Figure 3a).
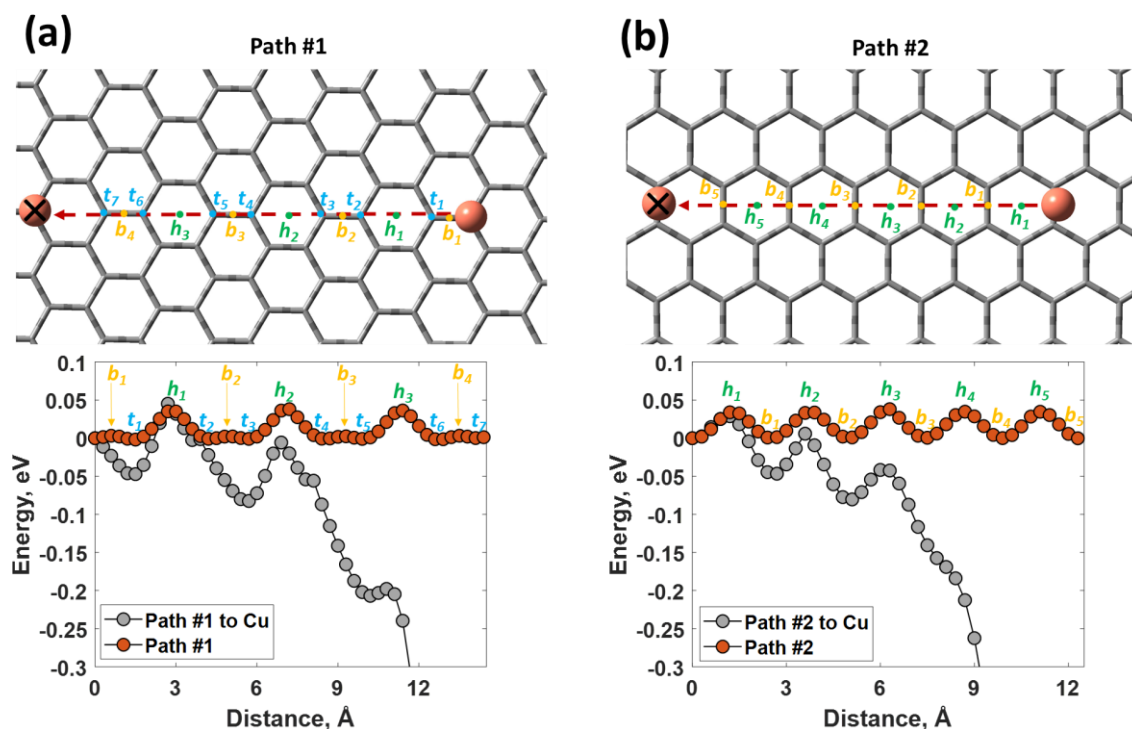
Figure 5. Potential energy curves for the movement of metallic copper atoms along the path #1 (**a**) and path #2 (**b**) in the presence and in the absence (marked by cross) of another copper atom. The height of the Cu atom was set to 2.723 Å. Note: the potential energy curve was normalized to the total energy of the system with a copper atom located at the top site of the graphene (energetically the most favorable site for copper adsorption); t_i, b_i and h_i designate the possible sites (top, bridge and hollow, respectively) that are available for copper atom adsorption.

4. Conclusions

In this work, we have clarified the fundamental mechanisms behind the Cu electroreduction and kinetics at the epitaxial graphene/4H-SiC (0001) working electrode. We demonstrated and discussed the results of cyclic voltammetry, chronoamperometry, and DFT calculations in order to unravel the behavior of copper. The significant overpotential, typical of general faradaic phenomena, on epitaxial graphene yielded a bi-electronic reduction in copper ions bypassing Cu^{1+} intermediates. The dynamic electrochemical measurements revealed an instantaneous nucleation mechanism, implying a limited number of active sites available for the deposit's growth, which seems to be akin to other metal (e.g., Pb, Hg and Li) electrodeposition on epitaxial graphene. In particular, it was revealed that the electrodeposition of metallic copper was possible only at two potentials (−0.39 and −0.4 V), as evidenced by the shape of the corresponding current transients. The estimated diffusion coefficient (~4.97–5.32 × 10^{-5} cm²/s) from the electrolyte to the EG electrode and the nuclei population density (~1.38–1.55 × 10^6 cm⁻²) is consistent with data from the literature and indicates that the epitaxial graphene electrode is suitable for fast and Cu electroplating. By performing DFT calculations, we modelled the diffusion of the Cu on graphene and showed that, independently of the diffusion paths, there is a small barrier (35 meV) for the surface migration of Cu, which disappears in the presence of another Cu atom in close proximity to the first one. This favors the mass transfer within the diffusion zones and a fast nucleation process. The obtained results shed light on the nature of the copper electroreduction process at the epitaxial graphene and may facilitate the development of real applications based on copper–graphene nanohybrid materials.

Supplementary Materials: The following are available online at http://www.mdpi.com/2076-3417/10/4/1405/s1, Figure S1: The decrease of the computed electron acceptor reactivity with the addition of the water molecules into

the aquo complexes. Figure S2: The change in Hirshfeld charge on Cu species with the addition of the water molecules into the aquo complexes.

Author Contributions: Conceptualization, I.S. and M.V.; methodology, I.S. and M.V.; software, I.S.; validation, I.S., M.V. and R.Y.; formal analysis, I.S.; investigation, I.S. and M.V.; resources, I.S., M.V. and R.Y.; data curation, I.S.; writing—original draft preparation, I.S.; writing—review and editing, I.S., M.V. and R.Y.; visualization, I.S.; supervision, R.Y.; project administration, R.Y.; funding acquisition, I.S. and R.Y. All authors have read and agreed to the published version of the manuscript.

Funding: The authors would like to thank the Swedish Foundation for Strategic research (SSF) for financial support through the grants GMT14-0077 and RMA15-024. I.S. acknowledges the support from Ångpanneföreningens Forskningsstiftelse (Grant 16-541). R.S. acknowledges financial support via VR grant 2018-04962.

Conflicts of Interest: The authors declare no conflict of interest.

References

1. Hu, C.-K.; Harper, J.M.E. Copper interconnections and reliability. *Mater. Chem. Phys.* **1998**, *52*, 5–16. [CrossRef]

2. Liu, H.; Favier, F.; Ng, K.; Zach, M.P.; Penner, R.M. Size-selective electrodeposition of meso-scale metal particles: A general method. *Electrochim. Acta* **2001**, *47*, 671. [CrossRef]

3. Grujicic, D.; Pesic, B. Electrodeposition of copper: The nucleation mechanisms. *Electrochim. Acta* **2002**, *47*, 2901. [CrossRef]

4. Ghodbane, O.; Roue, L.; Belanger, D. Copper electrodeposition on pyrolytic graphite electrodes: Effect of the copper salt on the electrodeposition process. *Electrochim. Acta* **2007**, *52*, 5843. [CrossRef]

5. Brownson, D.A.C.; Kampouris, D.K.; Banks, C.E. Graphene electrochemistry: Fundamental concepts through to prominent applications. *Chem. Soc. Rev.* **2012**, *41*, 6944. [CrossRef] [PubMed]

6. McCreery, R.L. Advanced carbon electrode materials for molecular electrochemistry. *Chem. Rev.* **2008**, *108*, 2646–2687. [CrossRef] [PubMed]

7. Virojanadara, C.; Syväjarvi, M.; Yakimova, R.; Johansson, L.I.; Zakharov, A.A.; Balasubramanian, T. Homogeneous large-area graphene layer growth on 6H-SiC (0001). *Phys. Rev. B* **2008**, *78*, 245403. [CrossRef]

8. An, Z.; Li, J.; Kikuchi, A.; Wang, Z.; Jiang, Y.; Ono, T. Mechanically strengthened graphene–Cu composite with reduced thermal expansion towards interconnect applications. *Microsyst. Nanoeng.* **2019**, *5*, 20. [CrossRef]

9. Cui, R.; Han, Y.; Zhu, Z.; Chen, B.; Ding, Y.; Zhang, Q.; Wang, Q.; Ma, G.; Pei, F.; Ye, Z. Investigation of the structure and properties of electrodeposited Cu/graphene composite coatings for the electrical contact materials of an ultrahigh voltage circuit breaker. *J. Alloy. Compd.* **2019**, *777*, 1159–1167. [CrossRef]

10. Maharana, H.S.; Rai, P.K.; Basu, A. Surface-mechanical and electrical properties of pulse electrodeposited Cu–graphene oxide composite coating for electrical contacts. *J. Mater. Sci.* **2017**, *52*, 1089–1105. [CrossRef]

11. Hidalgo-Manrique, P.; Lei, X.; Xu, R.; Zhou, M.; Kinloch, I.A.; Young, R.J. Copper/graphene composites: A review. *J. Mater. Sci.* **2019**, *54*, 12236. [CrossRef]

12. Sookhakian, M.; Ridwan, N.A.; Zalnezhad, E.; Yoon, G.H.; Azarang, M.; Mahmoudian, M.R.; Alias, Y. Layer-by-layer electrodeposited reduced graphene oxide-copper nanopolyhedra films as efficient platinum-free counter electrodes in high efficiency dye-sensitized solar cells. *J. Electrochem. Soc.* **2016**, *163*, D154–D159. [CrossRef]

13. Givalou, L.; Tsichlis, D.; Zhang, F.; Karagianni, C.-S.; Terrones, M.; Kordatos, K.; Falaras, P. Transition metal—Graphene oxide nanohybrid materials as counter electrodes for high efficiency quantum dot solar cells. *Catal. Today* **2019**. [CrossRef]

14. Kamboj, A.; Raghupathy, Y.; Rekha, M.Y.; Srivastava, C. Morphology, texture and corrosion behavior of nanocrystalline copper–graphene composite coatings. *JOM* **2017**, *69*, 1149–1154. [CrossRef]

15. Raghupathy, Y.; Kamboj, A.; Rekha, M.Y.; Narasimha Rao, N.P.; Srivastava, C. Copper–graphene oxide composite coatings for corrosion protection of mild steel in 3.5% NaCl. *Thin Solid Film* **2017**, *636*, 107–115. [CrossRef]

16. Li, S.; Song, G.; Fu, Q.; Pan, C. Preparation of Cu- graphene coating via electroless plating for high mechanical property and corrosive resistance. *J. Alloy. Compd.* **2019**, *777*, 877–885. [CrossRef]

17. Protich, Z.; Santhanam, K.S.V.; Jaikumar, A.; Kandlikar, S.G.; Wong, P. Electrochemical deposition of copper in graphene quantum dot bath: Pool boiling enhancement. *J. Electrochem. Soc.* **2016**, *163*, E166–E172. [CrossRef]

18. Jaykumar, A.; Santhanam, K.S.V.; Kandlikar, S.; Raya, I.B.P.; Raghupathi, P. Electrochemical deposition of copper on graphene with a high heat transfer coefficient. *ECS Trans.* **2015**, *66*, 55. [CrossRef]

19. Zhu, L.; Guo, X.; Liu, Y.; Chen, Z.; Zhang, W.; Yin, K.; Li, L.; Zhang, Y.; Wang, Z.; Sun, L. High-performance Cu nanoparticles/three-dimensional graphene/Ni foam hybrid for catalytic and sensing applications. *Nanotechnology* **2018**, *29*, 145703. [CrossRef]

20. Qin, L.; Xu, H.; Zhu, K.; Kang, S.-Z.; Li, G.; Li, X. Noble-metal-free copper nanoparticles/reduced graphene oxide composite: A new and highly efficient catalyst for transformation of 4-Nitrophenol. *Catal. Lett.* **2017**, *147*, 1315–1321. [CrossRef]

21. Gao, H.; Wang, Y.; Xiao, F.; Ching, C.B.; Duan, H. Growth of copper nanocubes on graphene paper as free-standing electrodes for direct hydrazine fuel cells. *J. Phys. Chem. C* **2012**, *116*, 7719–7725. [CrossRef]

22. Liu, C.; Zhang, H.; Tang, Y.; Luo, S. Controllable growth of graphene/Cu composite and its nanoarchitecture-dependent electrocatalytic activity to hydrazine oxidation. *J. Mater. Chem. A* **2014**, *2*, 4580–4587. [CrossRef]

23. Periasamy, A.P.; Liu, J.; Lin, H.-M.; Chang, H.-T. Synthesis of copper nanowire decorated reduced graphene oxide for electro-oxidation of methanol. *J. Mater. Chem. A* **2013**, *1*, 5973–5981. [CrossRef]

24. Muralikrishna, S.; Ravishankar, T.N.; Ramakrishnappa, T.; Nagaraju, D.H.; Krishna Pai, R. Non-noble metal graphene oxide-copper (II) ions hybrid electrodes for electrocatalytic hydrogen evolution reaction. *Environ. Prog. Sustain. Energy* **2016**, *35*, 565–573. [CrossRef]

25. He, T.; Zhang, C.; Du, A. Single-atom supported on graphene grain boundary as an efficient electrocatalyst for hydrogen evolution reaction. *Chem. Eng. Sci.* **2019**, *194*, 58–63. [CrossRef]

26. Yuan, J.; Yang, M.-P.; Zhi, W.-Y.; Wang, H.; Wang, H.; Lu, J.-X. Efficient electrochemical reduction of CO_2 to ethanol on Cu nanoparticles decorated on N-doped graphene oxide catalysts. *J. CO2 Util.* **2019**, *33*, 452–460. [CrossRef]

27. Shi, R.; Zhao, J.; Liu, S.; Sun, W.; Li, H.; Hao, P.; Li, Z.; Ren, J. Nitrogen-doped graphene supported copper catalysts for methanol oxidative carbonylation: Enhancement of catalytic activity and stability by nitrogen species. *Carbon* **2018**, *130*, 185–195. [CrossRef]

28. Sirijaraensre, J.; Khongpracha, P.; Limtrakul, J. Mechanistic insights into CO_2 cycloaddition to propylene oxide over a single copper atom incorporated graphene-based materials: A theoretical study. *Appl. Surf. Sci.* **2019**, *470*, 755–763. [CrossRef]

29. Sredojević, D.N.; Šljivančanin, Ž.; Brothers, E.N.; Belić, M.R. Formic Acid Synthesis by CO_2 Hydrogenation over Single-Atom Catalysts Based on Ru and Cu Embedded in Graphene. *Chem. Sel.* **2018**, *3*, 2631–2637. [CrossRef]

30. Back, S.; Lim, J.; Kim, N.-Y.; Kim, Y.-H.; Jung, Y. Single-atom catalysts for CO_2 electroreduction with significant activity and selectivity improvements. *Chem. Sci.* **2017**, *8*, 1090–1096. [CrossRef]

31. Öztürk Doğan, H.; Kurt Urhan, B.; Çepni, E.; Eryiğit, M. Simultaneous electrochemical detection of ascorbic acid and dopamine on Cu_2O/CuO/electrochemically reduced graphene oxide (CuxO/ERGO)-nanocomposite-modified electrode. *Microchem. J.* **2019**, *150*, 104157. [CrossRef]

32. Fu, J.; An, X.; Yao, Y.; Guo, Y.; Sun, X. Electrochemical aptasensor based on one step co-electrodeposition of aptamer and GO-CuNPs nanocomposite for organophosphorus pesticide detection. *Sens. Actuators B* **2019**, *287*, 503–509. [CrossRef]

33. Li, D.; Wang, C.; Zhang, H.; Sun, Y.; Duan, Q.; Ji, J.; Zhang, W.; Sang, S. A highly effective copper nanoparticle coupled with RGO for electrochemical detection of heavy metal ions. *Int. J. Electrochem. Sci.* **2017**, *12*, 10933–10945. [CrossRef]

34. Liu, C.; Qiao, C. Preparation of graphene-copper nanocomposite for electrochemical determination of cadmium ions in water. *Int. J. Electrochem. Sci.* **2017**, *12*, 8357–8367. [CrossRef]

35. Cui, D.; Su, L.; Li, H.; Li, M.; Li, C.; Xu, S.; Qian, L.; Yang, B. Non-enzymatic glucose sensor based on micro-/nanostructured Cu/Ni deposited on graphene sheets. *J. Electroanal. Chem.* **2019**, *838*, 154–162. [CrossRef]

36. Jiang, J.; Zhang, P.; Liu, Y.; Luo, H. A novel non-enzymatic glucose sensor based on a Cu-nanoparticle-modified graphene edge nanoelectrode. *Anal. Methods* **2017**, *9*, 2205–2210. [CrossRef]

37. Luo, J.; Jiang, S.; Zhang, H.; Jiang, J.; Liu, X. A novel non-enzymatic glucose sensor based on Cu nanoparticle modified graphene sheets electrode. *Anal. Chim. Acta* **2012**, *709*, 47–53. [CrossRef]

38. Balasubramanian, P.; Velmurugan, M.; Chen, S.-M.; Hwa, K.-Y. Optimized electrochemical synthesis of copper nanoparticles decorated reduced graphene oxide: Application for enzymeless determination of glucose in human blood. *J. Electroanal. Chem.* **2017**, *807*, 128–136. [CrossRef]

39. Shabnam, L.; Faisal, S.N.; Roy, A.K.; Haque, E.; Minett, A.I.; Gomes, V.G. Doped graphene/Cu nanocomposite: A high sensitivity non-enzymatic glucose sensor for food. *Food Chem.* **2017**, *221*, 751–759. [CrossRef]

40. Yang, Y.; Ma, N.; Bian, Z. Cu-Au/rGO nanoparticle based electrochemical sensor for 4-chlorophenol detection. *Int. J. Electrochem. Sci.* **2019**, *14*, 4095–4113. [CrossRef]

41. Dorraji, P.S.; Jalali, F. A nanocomposite of poly(melamine) and electrochemically reduced graphene oxide decorated with Cu nanoparticles: Application to simultaneous determination of hydroquinone and catechol. *J. Electrochem. Soc.* **2015**, *162*, B237–B244. [CrossRef]

42. Wang, H.; Wang, C.; Yang, B.; Zhai, C.; Bin, D.; Zhang, K.; Yang, P.; Du, Y. A facile fabrication of copper particle-decorated novel graphene flower composites for enhanced detecting of nitrite. *Analyst* **2015**, *140*, 1291–1297. [CrossRef] [PubMed]

43. Majidi, M.R.; Ghaderi, S. Hydrogen bubble dynamic template fabrication of nanoporous Cu film supported by graphene nanosheets: A highly sensitive sensor for detection of nitrite. *Talanta* **2017**, *175*, 21–29. [CrossRef] [PubMed]

44. Su, Z.; Tan, L.; Yang, R.; Zhang, Y.; Tao, J.; Zhang, N.; Wen, F. Cu-modified carbon spheres/reduced graphene oxide as a high sensitivity of gas sensor for NO2 detection at room temperature. *Chem. Phys. Lett.* **2018**, *695*, 153–157. [CrossRef]

45. Muralikrishna, S.; Cheunkar, S.; Lertanantawong, B.; Ramakrishnappa, T.; Nagaraju, D.H.; Surareungchai, W.; Balakrishna, R.G.; Reddy, K.R. Graphene oxide-Cu(II) composite electrode for non-enzymatic determination of hydrogen peroxide. *J. Electroanal. Chem.* **2016**, *776*, 9–65. [CrossRef]

46. Zhou, Q.; Su, X.; Ju, W.; Yong, Y.; Li, X.; Fu, Z.; Wang, C. Adsorption of H2S on graphane decorated with Fe, Co and Cu: A DFT study. *RSC Adv.* **2017**, *7*, 31457–31465. [CrossRef]

47. Mohammadi-Manesh, E.; Vaezzadeh, M.; Saeidi, M. Cu- and CuO-decorated graphene as a nanosensor for H2S detection at room temperature. *Surf. Sci.* **2015**, *636*, 36–41. [CrossRef]

48. Zheng, J.H.; Niu, S.F.; Lian, J.S. Carbon monoxide adsorption on cooper doped graphene systems: A DFT study. *Optoelectron. Adv. Mater. Rapid Commun.* **2014**, *8*, 1044–1049.

49. Li, X.; Chen, X.; Qi, J. First-principle theory calculations of CO_2 adsorption and activation by metal-graphene composite. *Harbin Gongye Daxue Xuebao J. Harbin Inst. Technol.* **2014**, *46*, 58–64.

50. Liu, Z.; Cheng, X.; Yang, Y.; Jia, H.; Bai, B.; Zhao, L. DFT study of N_2O adsorption onto the surface of M -decorated graphene oxide (M. = Mg, Cu or Ag). *Materials* **2019**, *12*, 2611. [CrossRef]

51. Choudhary, A.; Malakkal, L.; Siripurapu, R.K.; Szpunar, B.; Szpunar, J. First principles calculations of hydrogen storage on Cu and Pd-decorated graphene. *Int. J. Hydrog. Energy* **2016**, *41*, 17652–17656. [CrossRef]

52. Wong, J.; Yadav, S.; Tam, J.; Veer Singh, C. A van der Waals density functional theory comparison of metal decorated graphene systems for hydrogen adsorption. *J. Appl. Phys.* **2014**, *115*, 224301. [CrossRef]

53. Sigal, A.; Rojas, M.I.; Leiva, E.P.M. Is hydrogen storage possible in metal-doped graphite 2D systems in conditions found on earth? *Phys. Rev. Lett.* **2011**, *107*, 158701. [CrossRef] [PubMed]

54. Malček, M.; Cordeiro, M.N.D.S. A DFT and QTAIM study of the adsorption of organic molecules over the copper-doped coronene and circumcoronene. *Phys. E* **2018**, *95*, 59–70. [CrossRef]

55. Malček, M.; Bučinský, L.; Teixeira, F.; Cordeiro, M.N.D.S. Detection of simple inorganic and organic molecules over Cu-decorated circumcoronene: A combined DFT and QTAIM study. *Phys. Chem. Chem. Phys.* **2018**, *20*, 16021–16032. [CrossRef]

56. Düzenli, D.A. Comparative density functional study of hydrogen peroxide adsorption and activation on the graphene surface doped with N, B, S, Pd, Pt, Au, Ag, and Cu Atoms. *J. Phys. Chem. C* **2016**, *120*, 20149–20157. [CrossRef]

57. National Research Council (US) Committee on Copper in Drinking Water. *Copper in Drinking Water*; Health Effects of Excess Copper; National Academies Press: Washington, DC, USA, 2000; p. 5.

58. Brewer, G.J. Alzheimer's disease causation by copper toxicity and treatment with zinc. *Front. Aging Neurosci.* **2014**, *16*, 92. [CrossRef]

59. Schedin, F.; Geim, A.K.; Morozov, S.V.; Hill, E.W.; Blake, P.; Katsnelson, M.I.; Novoselov, K.S.; Morozov, S.; Novoselov, K. Detection of individual gas molecules adsorbed on graphene. *Nat. Mater.* **2007**, *6*, 652–655. [CrossRef]

60. Yang, T.; Zhao, X.; He, Y.; Zhu, H. *Graphene-Based Sensors*; Elsevier BV: Amsterdam, The Netherlands, 2018; pp. 157–174.

61. Molina, J.; Cases, F.; Moretto, L.M. Graphene-based materials for the electrochemical determination of hazardous ions. *Anal. Chim. Acta* **2016**, *946*, 9–39. [CrossRef]

62. Petsawi, P.; Yaiwong, P.; Laocharoensuk, R.; Ounnunkad, K. Determination of copper (II) and cadmium (II) in rice samples by anodic stripping square wave voltammetry using reduced graphene oxide/polypyrrole composite modified screen-printed carbon electrode. *Chiang Mai J. Sci.* **2019**, *46*, 322–336.

63. Tian, X.; Tan, Z.; Zhang, Z.; Zhan, T.; Liu, X. An electrochemical sensor based on an ionic liquid covalently functionalized graphene oxide for simultaneous determination of copper (II) and antimony (III). *Chem. Sel.* **2018**, *3*, 8252–8258. [CrossRef]

64. Ahour, F.; Taheri, M. Anodic stripping voltammetric determination of copper (II) ions at a graphene quantum dot-modified pencil graphite electrode. *J. Iran. Chem. Soc.* **2018**, *15*, 343–350. [CrossRef]

65. Wang, Y.; Zhao, S.; Li, M.; Li, W.; Zhao, Y.; Qi, J.; Cui, X. Graphene quantum dots decorated graphene as an enhanced sensing platform for sensitive and selective detection of copper (II). *J. Electroanal. Chem.* **2017**, *797*, 113–120. [CrossRef]

66. Sun, H.; Jia, Y.; Dong, H.; Fan, L. Graphene oxide nanosheets coupled with paper microfluidics for enhanced on-site airborne trace metal detection. *Microsyst. Nanoeng.* **2019**, *5*, 4. [CrossRef]

67. Zhang, Y.; Li, K.; Ren, S.; Dang, Y.; Liu, G.; Zhang, R.; Zhang, K.; Long, X.; Jia, K. Coal-derived graphene quantum dots produced by ultrasonic physical tailoring and their capacity for Cu(II) detection. *ACS Sustain. Chem. Eng.* **2019**, *7*, 9793–9799. [CrossRef]

68. Akhila, A.K.; Renuka, N.K. Coumarin-graphene turn-on fluorescent probe for femtomolar level detection of copper(ii). *N. J. Chem.* **2019**, *43*, 1001–1008. [CrossRef]

69. Nazerdeylami, S.; Ghasemi, J.B.; Badiei, A. Anthracene modified graphene oxide-silica as an optical sensor for selective detection of Cu2+ and I− ions. *Int. J. Environ. Anal. Chem.* **2019**, 1–16. [CrossRef]

70. Basiri, S.; Mehdinia, A.; Jabbari, A. Green synthesis of reduced graphene oxide-Ag nanoparticles as a dual-responsive colorimetric platform for detection of dopamine and Cu2+. *Sens. Actuators B* **2018**, *262*, 499–507. [CrossRef]

71. Wang, C.; Yang, F.; Tang, Y.; Yang, W.; Zhong, H.; Yu, C.; Li, R.; Zhou, H.; Li, Y.; Mao, L. Graphene quantum dots nanosensor derived from 3D nanomesh graphene frameworks and its application for fluorescent sensing of Cu 2+ in rat brain. *Sens. Actuators B* **2018**, *258*, 672–681. [CrossRef]

72. Song, F.; Ai, Y.; Zhong, W.; Wang, J. Detection of copper ions and glutathione based on off-on fluorescent graphene quantum dots. *J. China. Pharm. Univ.* **2018**, *49*, 87–92. [CrossRef]

73. Li, M.; Liu, Z.; Wang, S.; Calatayud, D.G.; Zhu, W.-H.; James, T.D.; Wang, L.; Mao, B.; Xiao, H.-N. Fluorescence detection and removal of copper from water using a biobased and biodegradable 2D soft material. *Chem. Commun.* **2018**, *54*, 184–187. [CrossRef] [PubMed]

74. Zheng, W.; Li, H.; Chen, W.; Zhang, J.; Wang, N.; Guo, X.; Jiang, X. Rapid detection of copper in biological systems using click chemistry. *Small* **2018**, *14*, 1703857. [CrossRef] [PubMed]

75. Shtepliuk, I.; Khranovskyy, V.; Yakimova, R. Combining graphene with silicon carbide: Synthesis and properties—A review. *Semicond. Sci. Technol.* **2016**, *31*, 113004. [CrossRef]

76. Shtepliuk, I.; Iakimov, T.; Khranovskyy, V.; Eriksson, J.; Giannazzo, F.; Yakimova, R. Role of the Potential Barrier in the Electrical Performance of the Graphene/SiC Interface. *Crystals* **2017**, *7*, 162. [CrossRef]

77. Yazdi, G.R.; Iakimov, T.; Yakimova, R. Epitaxial Graphene on SiC: A Review of Growth and Characterization. *Crystals* **2016**, *6*, 53. [CrossRef]

78. Shtepliuk, I.; Santangelo, M.F.; Vagin, M.; Ivanov, I.G.; Khranovskyy, V.; Iakimov, T.; Eriksson, J.; Yakimova, R. Understanding Graphene response to neutral and charged lead species: Theory and experiment. *Materials* **2018**, *11*, 2059. [CrossRef]

79. Santangelo, M.F.; Shtepliuk, I.; Filippini, D.; Ivanov, I.G.; Yakimova, R.; Eriksson, J. Real-time sensing of lead with epitaxial graphene-integrated microfluidic devices. *Sens. Actuators B* **2019**, *288*, 425–431. [CrossRef]

80. Shtepliuk, I.; Vagin, M.; Yakimova, R. Insights into the Electrochemical Behavior of Mercury on Graphene/SiC Electrodes. *C J. Carbon Res.* **2019**, *5*, 51. [CrossRef]

81. Yakimova, R.; Iakimov, T.; Syväjärvi, M. Process for Growth of Graphene. U.S. Patent US9150417B2, 6 October 2015.

82. Ivanov, I.G.; Hassan, J.U.; Iakimov, T.; Zakharov, A.A.; Yakimova, R.; Janzén, E. Layer-number determination in graphene on SiC by reflectance mapping. *Carbon* **2014**, *77*, 492–500. [CrossRef]

83. Vagin, M.Y.; Sekretaryova, A.N.; Ivanov, I.G.; Håkansson, A.; Iakimov, T.; Syväjärvi, M.; Yakimova, R.; Lundström, I.; Eriksson, M. Monitoring of epitaxial graphene anodization. *Electrochim. Acta* **2017**, *238*, 91–98. [CrossRef]

84. Yamaguchi, T.; Nomura, M.; Wakita, H.; Ohtaki, H. An extended x-ray absorption fine structure study of aqueous rare earth perchlorate solutions in liquid and glassy states. *J. Chem. Phys.* **1988**, *89*, 5153–5159. [CrossRef]

85. Sémon, L.; Boehme, C.; Billard, I.; Hennig, C.; Lützenkirchen, K.; Reich, T.; Rossini, I.; Wipff, G.; Roßberg, A.; Roßberg, A. Do Perchlorate and Triflate Anions Bind to the Uranyl Cation in an Acidic Aqueous Medium? A Combined EXAFS and Quantum Mechanical Investigation. *Chem. Phys. Chem.* **2001**, *2*, 591–598. [CrossRef]

86. Binnemans, K. Applications of tetravalent cerium compounds. In *Handbook on the Physics and Chemistry of Rare Earths*, 1st ed.; Gschneidner, K.A., Jr., Bünzli, J.-C.G., Pecharsky, V.K., Eds.; Elsevier: Amsterdam, The Netherlands, 2006; Volume 3, pp. 306–307. ISBN 9780080466729.

87. Scharifker, B.; Hills, G. Theoretical and experimental studies of multiple nucleation. *Electrochim. Acta* **1983**, *28*, 879–889. [CrossRef]

88. Frisch, M.J. Gaussian 16. In *Revision, B. 01*; Gaussian Inc.: Wallingford, CT, USA, 2016.

89. Adamo, C.; Barone, V. Toward reliable density functional methods without adjustable parameters: The PBE0 model. *J. Chem. Phys.* **1999**, *110*, 6158–6170. [CrossRef]

90. Perdew, J.P.; Burke, K.; Ernzerhof, M. Generalized Gradient Approximation Made Simple. *Phys. Rev. Lett.* **1996**, *77*, 3865–3868. [CrossRef]

91. Martin, G.; Sundermann, A. Correlation consistent valence basis sets for use with the Stuttgart–Dresden–Bonn relativistic effective core potentials: The atoms Ga–Kr and In–Xe. *J. Chem. Phys.* **2001**, *114*, 3408–3420. [CrossRef]

92. Lu, T.; Chen, F. Multiwfn: A multifunctional wavefunction analyzer. *J. Comput. Chem.* **2012**, *33*, 580–592. [CrossRef]

93. Santangelo, M.F.; Shtepliuk, I.; Filippini, D.; Puglisi, D.; Vagin, M.; Yakimova, R.; Eriksson, J. Epitaxial Graphene sensors combined with 3D-printed microfluidic chip for heavy metals detection. *Sensors* **2019**, *19*, 2393. [CrossRef]

94. Abbott, A.P.; El Ttaib, K.; Frisch, G.; McKenzie, K.J.; Ryder, K.S. Electrodeposition of copper composites from deep eutectic solvents based on choline chloride. *Phys. Chem. Chem. Phys.* **2009**, *11*, 4269–4277. [CrossRef]

95. Sebastian, P.; Valles, E.; Gomez, E. Copper electrodeposition in a deep eutectic solvent. First stages analysis considering Cu(I) stabilization in chloride media. *Electrochim. Acta* **2014**, *123*, 285–295. [CrossRef]

96. Jovic, V.D.; Jovic, G.M. Copper electrodeposition from a copper acid baths in the presence of PEG and NaCl. *J. Serb. Chem. Soc.* **2001**, *66*, 935–952. [CrossRef]

97. Che, C.Y.; Vagin, M.; Wijeratne, K.; Zhao, D.; Warczak, M.; Jonsson, M.P.; Crispin, X. Conducting polymer electrocatalysts for proton-coupled electron transfer reactions: Toward organic fuel cells with forest fuels. *Adv. Sustain. Syst.* **2018**, *2*, 1800021. [CrossRef]

98. Persson, I.; Persson, P.; Sandström, M.; Ullström, A.-S. Structure of Jahn–Teller distorted solvate copper (II) ions in solution, and in solids with apparently regular octahedral coordination geometry. *Chem. Soc. Dalton Trans.* **2002**, *7*, 1256–1265. [CrossRef]

99. Li, J.; Fisher, C.L.; Chen, J.L.; Bashford, D.; Noodleman, L. Calculation of redox potentials and pKa values of hydrated transition metal cations by a combined density functional and continuum dielectric theory. *Inorg. Chem.* **1996**, *35*, 4694. [CrossRef]

100. Smith, E.L.; Barron, J.C.; Abbott, A.P.; Ryder, K.S. Time resolved in situ liquidatomic force microscopy and simultaneous acoustic impedance electrochemical quartz crystal microbalance measurements: A study of Zn deposition. *Anal. Chem.* **2009**, *81*, 8466–8471. [CrossRef]

101. Shtepliuk, I.; Vagin, M.; Ivanov, I.G.; Iakimov, T.; Yazdi, G.R.; Yakimova, R. Lead (Pb) interfacing with epitaxial graphene. *Phys. Chem. Chem. Phys.* **2018**, *20*, 17105–17116. [CrossRef]

102.　Ziegler, C.; Wielgosz, R.I.; Kolb, D.M. Pb deposition on n-Si (111) electrodes. *Electrochim. Acta* **1999**, *45*, 827–833. [CrossRef]

103.　Tułodziecki, M.; Tarascona, J.-M.; Tabernab, P.L.; Guérya, C. Importance of the double layer structure in the electrochemicaldeposition of Co from soluble Co2+- based precursors in Ionic Liquid media. *Electrochim. Acta* **2014**, *134*, 55–66. [CrossRef]